Inner-Loop Control of Fixed-Wing Unmanned Aerial Vehicles in Icing Conditions

Sif Högnadottir*, Kristoffer Gryte†, Richard Hann‡ and Tor Arne Johansen§
Department of Engineering Cybernetics,
Center for Autonomous Marine Operations and Systems,
Norwegian University of Science and Technology,
Trondheim, Norway

This paper compares a model reference adaptive control (MRAC) scheme with PID controllers. Both are developed for the Skywalker X8 fixed-wing unmanned aerial vehicle operating in icing conditions, encompassing asymmetric icing on the wings and reduced control effectiveness. The MRAC scheme is given by a linear model with a bias term to capture unmodeled effects, and modified with the projection operator to increase robustness. The findings in this paper show that the MRAC control scheme and the PID controller demonstrate similar qualities in tracking performance with the MRAC performing better under certain conditions. Overall, both controllers exhibit the most difficulty when the icing level is severely asymmetric. Examining the bias and integral terms of the adaptive controller and PID controller, respectively, shows that the bias terms when the adaptive rate is lowered, and to some degree the roll integral term, are able to detect icing.

I. Nomenclature

ρ	=	Air density
V_a	=	Airspeed
b	=	Wing span
c	=	Chord length
α	=	Angle of attack
β	=	Sideslip angle
ϕ	=	Roll angle
θ	=	Pitch angle
p	=	Roll rate
q	=	Pitch rate
r	=	Yaw rate
δ_a	=	Aileron deflection
δ_e	=	Elevator deflection
δ_r	=	Rudder deflection
δ_t	=	Throttle input
l	=	Roll moment
m	=	Pitch moment
n	=	Yaw moment
C_D	=	Aerodynamic drag coefficient
C_S	=	Aerodynamic side force coefficient
C_L	=	Aerodynamic lift coefficient
C_l	=	Aerodynamic roll moment coefficient
C_m	=	Aerodynamic pitch moment coefficient
C_n	=	Aerodynamic yaw moment coefficient
ζ	=	Icing level
$\boldsymbol{l}_k$	=	Point of attack on the left wing
$\boldsymbol{r}_k$	=	Point of attack on the right wing
$\boldsymbol{x}$	=	MRAC system state
$\boldsymbol{u}$	=	MRAC control input
$\boldsymbol{A}$	=	MRAC system matrix
$\boldsymbol{B}$	=	MRAC control matrix
$\boldsymbol{\Phi}(\boldsymbol{x})$	=	MRAC regressor vector
$\boldsymbol{P}$	=	Solution to the Lyapunov equation
$\boldsymbol{\Gamma}_*$	=	Adaptive rate
k_{p_*}	=	PID proportional gain
k_{i_*}	=	PID integral gain
k_{d_*}	=	PID derivative gain

*MSc. student, Department of Engineering Cybernetics, Norwegian University of Science and Technology (NTNU), Trondheim, Norway
†Researcher, Department of Engineering Cybernetics, Norwegian University of Science and Technology (NTNU), Trondheim, Norway
‡Researcher, Department of Engineering Cybernetics, Norwegian University of Science and Technology (NTNU), Trondheim, Norway
§Professor, Department of Engineering Cybernetics, Norwegian University of Science and Technology (NTNU), Trondheim, Norway

II. Introduction

To widen the scope of admissible operations for the UAV, research is going into how the UAVs can handle different meteorological conditions. One of these conditions is flight in atmospheric icing conditions, which is the topic for this paper.

Icing is a debilitating factor to a UAV as it the increases drag, reduces the lift, and increases the risk of stalling [1]. These factors elicit the need for increased control efforts to maintain flight. Additionally, ice accretion or run-back icing on the wing surface ahead of control surfaces results in reduced control surface effectiveness [2]. Smaller aircraft, such as UAVs, are more sensitive to icing conditions compared to larger manned aircraft [3]. One way to handle icing conditions is using ice protection systems [4], that consist of *anti-icing* to prevent ice accretion, or *de-icing* to remove already formed ice. These systems necessitate an increase in power consumption and preferably knowledge of the icing level to optimize the ice removal and its energy consumption. The problem of automatic icing detection is still a research question. This is of more concern for UAVs than larger manned aircraft as UAVs must rely entirely on onboard sensors and instruments to detect icing, whereas larger manned aircraft have a pilot onboard that can identify icing conditions [5].

One approach is to combine the use of de-icing systems and controllers that can cope with the adverse effects of icing, thereby increasing the de-icing intervals and potentially reducing the associated energy consumption. Previous work has been done by Kleiven *et al.* [6] with the development of robust controllers in icing conditions for the fixed-wing Skywalker X8 UAV. In this paper, an adaptive control approach is explored for the Skywalker X8.

Adaptive control is a control scheme where the control law changes as an adaptive law attempts to estimate the parameters that characterize the system [7]. In this paper, an inner loop model reference adaptive control (MRAC) scheme is developed for attitude control. Model reference adaptive control is based on finding a feedback controller, such that the system output tracks a commanded reference, in the presence of unknown plant parameters. Similar research has been performed to test MRAC schemes on UAVs [8, 9].

Chowdhary presents in [8] an MRAC scheme for a fixed-wing UAV that has been subject to asymmetric structural damage. This motivates the development of an MRAC controller for operation in asymmetric icing conditions.

The controllers in this paper are tested in a simulation model in MATLAB/Simulink, wherein the model is based on the model data from the work of Winter *et al.* [10], with the extension to an asymmetric model from Kleiven *et al.* [6]. The aerodynamic coefficient data from [10] are given for iced and clean (no icing) airfoils. The icing data in [10] is found for the mixed icing case, being the most severe icing type of the three types – glaze, rime, and mixed – concerning aerodynamic performance. Since the aerodynamic coefficients are based on symmetric icing levels, there are some uncertainties in the model when extending it to an asymmetric icing model. However, it is assumed to give an adequate reflection of the UAV's behavior with respect to the control aspect and the dynamics of ice accretion and shedding [6]. As such, the model is assumed to be valid for this paper. Ice accretion on the propellers can have significant consequences on thrust generation [11]. However, ice accretion on the propellers is not considered in this paper.

This paper aims to answer the question of whether an adaptive solution is better suited to tackle the problem of controlling UAVs in icing conditions than a more conventional PID controller. Additionally, the paper aims to explore if one could infer any valuable knowledge about the icing conditions.

III. Aerodynamic Model

The aerodynamic model in this paper is described by a quasi-linear approximation of the aerodynamic coefficients,

$$\begin{bmatrix} F_{\text{drag}} \\ F_{\text{side}} \\ F_{\text{lift}} \end{bmatrix} = \bar{q}S \begin{bmatrix} C_D(\alpha) + C_{D_q}(\alpha)\frac{c}{2V_a}q + C_{D_{\delta_e}}\delta_e \\ C_S(\beta) + C_{S_p}(\beta)\frac{b}{2V_a}p + C_{S_r}(\beta)\frac{b}{2V_a}r + C_{S_{\delta_a}}\delta_a + C_{S_{\delta_r}}\delta_r \\ C_L(\alpha) + C_{L_q}(\alpha)\frac{c}{2V_a}q + C_{L_{\delta_e}}\delta_e \end{bmatrix}, \tag{1}$$

$$\begin{bmatrix} l \\ m \\ n \end{bmatrix} = \bar{q}S \begin{bmatrix} b\big(C_l(\beta) + C_{l_p}(\beta)\frac{b}{2V_a}p + C_{l_r}(\beta)\frac{b}{2V_a}r + C_{l_{\delta_a}}\delta_a + C_{l_{\delta_r}}\delta_r\big) \\ c\big(C_m(\alpha) + C_{m_q}(\alpha)\frac{c}{2V_a}q + C_{L_{\delta_e}}\delta_e\big) \\ b\big(C_n(\beta) + C_{n_p}(\beta)\frac{b}{2V_a}p + C_{n_r}(\beta)\frac{b}{2V_a}r + C_{n_{\delta_a}}\delta_a + C_{n_{\delta_r}}\delta_r\big) \end{bmatrix}, \tag{2}$$

where $\bar{q} = \frac{\rho V_a^2}{2}$. The nonlinear aerodynamic coefficients in eqs. (1) and (2) are interpolated values for a given angle of attack or sideslip based on aerodynamic data for the Skywalker X8 fixed-wing UAV found by Winter *et al.* [10]. Following the notation of Kleiven *et al.* in [6], the variable $\zeta \in [0, 1]$ is used to describe the level of icing. For the clean case $\zeta = 0$ and for the fully iced case $\zeta = 1$. The aerodynamic coefficients, C_k, are then found with linear interpolation as

$$C_k(\zeta) = \zeta \; C_{k,\text{iced}} + (1-\zeta)\; C_{k,\text{clean}}. \tag{3}$$

A. Extension to an Asymmetric Model

In [6], Kleiven *et al.* extended the symmetric model of the aircraft to an asymmetric model for the purpose of simulating asymmetric icing on the wings. The asymmetric model divides the aircraft into two parts, a left side and a right side. The asymmetry enters through the aerodynamic forces and moments. The total force acting through the center of mass of the aircraft is given by

$$\boldsymbol{F}_k = \boldsymbol{F}_{k,r} + \boldsymbol{F}_{k,l}, \tag{4}$$

where k is D, L or S, denoting the drag force, lift force and side force, respectively. The subscripts r and l denote the right and left side of the aircraft, respectively.

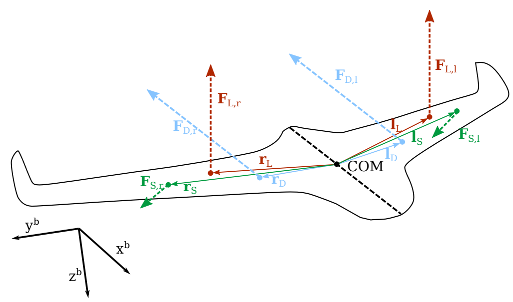

Figure 1 The forces of the asymmetric icing model. Courtesy of Kleiven [6].

The asymmetric aerodynamic moment is given in [6] by

$$\boldsymbol{m}_{a,\text{asym}} = \boldsymbol{m}_{a,0} + \sum_k (\boldsymbol{r}_k \times \boldsymbol{F}_{k,r} + \boldsymbol{l}_k \times \boldsymbol{F}_{l,r}) \quad \text{for } \boldsymbol{F}_{k,r}, \boldsymbol{F}_{k,l} \notin \boldsymbol{m}_{a,0}, \tag{5}$$

where $\boldsymbol{m}_{a,0}$ is a vector containing the symmetric moments l, m and n from eq. (2). The second term in eq. (5) is due to asymmetry in the corresponding aerodynamic forces on the left and right wing. The asymmetric forces are depicted in Fig. 1. The following assumptions are made by Kleiven *et al.* [6] with respect to the point of attack of the aerodynamic forces

- All points of attack are assumed to lie on the $\pm y$-axis.
- The icing level does not affect the points of attacks' y-coordinate.

IV. Icing

Atmospheric ice accretion on an aircraft can have a critical impact on the aerodynamics, causing a decrease in lift, an increase in drag, and reduced stall limit [2]. The stall limit is lowered as the ice formed on the airfoil causes the airflow to separate from the airfoil at a lower angle of attack. Moreover, the changes in lift and drag, imply that a greater thrust force is needed to compensate for the effects of icing. Hann *et al.* [3] shows that the smaller fixed-wing UAVs, compared to the larger and faster manned aircraft, are more affected by the ice accretion.

The three main types of icing conditions are glaze, rime, and mixed ice, wherein mixed icing lies in between the glaze and rime categorizations. Glaze ice occurs at temperatures from 0°C to −3°C, and they tend to have a rough surface and double horns, while rime ice occurs at temperatures below −10°C and tend to have a single horn and a relatively smooth surface [2]. By the findings of Hann in [12] mixed icing is considered the most severe type of icing condition concerning the degradation in aerodynamic effectiveness. [12] also shows that for the mixed icing the curve for the aerodynamic lift coefficient is shifted to the left. As a consequence, either the velocity of the UAV or the angle of attack must be increased to maintain its position in the flight envelope [12].

There are two main methods of icing protection to cope with ice accretion on the leading edge of the airfoil, namely de-icing and anti-icing methods. Anti-icing consists of continuously applying heat to the airfoils to prevent any icing from forming, whereas de-icing consists of periodically applying heat to remove already formed ice. Both require an increase in power consumption, although [4] suggests that anti-icing demands higher energy usage than de-icing in many conditions.

Further, ice accretion on the airfoils ahead of control surfaces such as ailerons, elevators, and rudders also results in a reduced control surface effectiveness [2]. The severity of the loss in control effectiveness is governed by three fluid dynamic properties described in [2]. In [6, 10], the icing is assumed to be on the leading edge only, and that the control surface on the trailing edge were unaffected by icing.

Through computational fluid dynamics (CFD) simulations, an estimate of the reduced control surface effectiveness due to icing on the airfoil is found for the longitudinal aerodynamics. The simulations are done with the ANSYS FENSAP-ICE simulation software and the method is described in the Appendix of this paper.

The analysis shows that the value of the aerodynamic coefficient $C_{L_{\delta_e}}$ is reduced by 27% from the clean to iced case, $C_{D_{\delta_e}}$ is increased by 86% and $C_{m_{\delta_e}}$ is reduced by 37%. Assuming that roll is only a function of the lift differential between the wings, and that yaw is only a function of the drag difference, the effects of reduced control surface effectiveness are incorporated into the lateral dynamics. Accordingly, the aerodynamic coefficient $C_{l_{\delta_a}}$ is reduced by 27% from the clean to iced case and $C_{n_{\delta_a}}$ is increased by 86%. It is noted that the CFD analysis is only used to determine the reduction in control effectiveness due to icing, while the rest of the model is the same as in Kleiven et al. [6].

V. Controller Design

A. Inner Loop Model Reference Adaptive Control

Based on Lavretsky and Wise [9], a model reference adaptive control scheme is developed for the UAV. Consider the nonlinear system

$$\dot{\boldsymbol{x}} = \boldsymbol{A}\boldsymbol{x} + \boldsymbol{B}\boldsymbol{\Lambda}(\boldsymbol{u} + f(\boldsymbol{x})), \tag{6}$$

where $\boldsymbol{x} \in \mathbb{R}^n$ is the state vector, $\boldsymbol{u} \in \mathbb{R}^m$ is the control input, $\boldsymbol{B} \in \mathbb{R}^{n\times m}$ is the known control matrix, $\boldsymbol{\Lambda} \in \mathbb{R}^{m\times m}$ is the unknown control effectiveness matrix and $\boldsymbol{A} \in \mathbb{R}^{n\times n}$ is the unknown state matrix. It is assumed that $f(\boldsymbol{x})$ can be written as

$$f(\boldsymbol{x}) = \boldsymbol{\Theta}^\top \Phi(\boldsymbol{x}), \tag{7}$$

where $\boldsymbol{\Theta} \in \mathbb{R}^{N\times m}$ is constant and unknown, and $\boldsymbol{\Phi}(\boldsymbol{x}) \in \mathbb{R}^N$ is the known regressor vector consisting of N locally Lipschitz-continuous basis functions [9]. The matrices $\boldsymbol{A}$ and $\boldsymbol{\Lambda}$ are assumed constant, and $\boldsymbol{\Lambda}$ is assumed to be diagonal with its elements $\lambda_i > 0$. Additionally, it is assumed that the pair $(\boldsymbol{A}, \boldsymbol{B}\boldsymbol{\Lambda})$ is controllable.

The control objective of the model reference adaptive controller is to have the system state in eq. (6) track the reference model

$$\dot{\boldsymbol{x}}_{\text{ref}} = \boldsymbol{A}_{\text{ref}}\boldsymbol{x}_{\text{ref}} + \boldsymbol{B}_{\text{ref}}\boldsymbol{r}(t), \tag{8}$$

driven by the commanded reference, $\boldsymbol{r}(t)$. The matrix is $\boldsymbol{A}_{\text{ref}} \in \mathbb{R}^{n\times n}$ is Hurwitz and $\boldsymbol{B}_{\text{ref}} \in \mathbb{R}^{n\times m}$ is the input matrix.

Tracking of the reference model is achieved with the control law

$$\boldsymbol{u} = \hat{\boldsymbol{K}}_{\boldsymbol{x}}{}^\top \boldsymbol{x} + \hat{\boldsymbol{K}}_{\boldsymbol{r}}{}^\top \boldsymbol{r} - \hat{\boldsymbol{\Theta}}^\top \boldsymbol{\Phi}(\boldsymbol{x}), \tag{9}$$

where $\hat{\boldsymbol{K}}_{\boldsymbol{x}} \in \mathbb{R}^{n\times m}$, $\hat{\boldsymbol{K}}_{\boldsymbol{r}} \in \mathbb{R}^{m\times m}$ and $\hat{\boldsymbol{\Theta}} \in \mathbb{R}^{N\times m}$ are controller gain matrices that will ensure tracking of the reference model dynamics and render the closed-loop error dynamics uniformly stable. The adaptive law for the controller gains are found through Lyapunov analysis in [9] and are given as,

$$\begin{aligned}
\dot{\hat{\boldsymbol{K}}}_x &= \text{Proj}(\hat{\boldsymbol{K}}_x,\ -\boldsymbol{\Gamma}_{\boldsymbol{x}}\boldsymbol{x}\boldsymbol{e}^\top \boldsymbol{P}\boldsymbol{B}), \\
\dot{\hat{\boldsymbol{K}}}_r &= \text{Proj}(\hat{\boldsymbol{K}}_r,\ -\boldsymbol{\Gamma}_{\boldsymbol{r}}\boldsymbol{r}\boldsymbol{e}^\top \boldsymbol{P}\boldsymbol{B}), \\
\dot{\hat{\boldsymbol{\Theta}}} &= \text{Proj}(\hat{\boldsymbol{\Theta}},\ \boldsymbol{\Gamma}_{\boldsymbol{\Theta}}\boldsymbol{\Phi}\boldsymbol{e}^\top \boldsymbol{P}\boldsymbol{B}),
\end{aligned} \tag{10}$$

where $\boldsymbol{\Gamma}_x = \boldsymbol{\Gamma}_x^\top > 0$, $\boldsymbol{\Gamma}_r = \boldsymbol{\Gamma}_r^\top > 0$ and $\boldsymbol{\Gamma}_\Theta = \boldsymbol{\Gamma}_\Theta^\top > 0$ are the adaptation rates, $\boldsymbol{e} = \boldsymbol{x} - \boldsymbol{x}_{\text{ref}}$, and where $\text{Proj}(\cdot)$ is the projection operator as defined in [9]. The matrix $\boldsymbol{P} = \boldsymbol{P}^\top > 0$ satisfies the algebraic Lyapunov equation

$$\boldsymbol{P}\boldsymbol{A}_{\text{ref}} + \boldsymbol{A}_{\text{ref}}^\top \boldsymbol{P} = -\boldsymbol{Q}, \tag{11}$$

for $\boldsymbol{Q} = \boldsymbol{Q}^\top > 0$.

1. Model equations

The model in the MRAC control scheme is chosen as a linear model with the addition of a bias term to capture nonlinear and unmodelled effects. From Beard & McLain [13], a linearization of the roll dynamics is given as

$$\begin{aligned}
\dot{\phi} &= p + d_{\phi_1}, \\
\ddot{\phi} &= -a_{\phi_1}\dot{\phi} + a_{\phi_2}\delta_a + d_{\phi_2},
\end{aligned} \tag{12}$$

where d_{ϕ_1} and d_{ϕ_2} consists of the unmodeled and nonlinear terms of the dynamics and are, for the linear model, considered as disturbances on the system. A model of the roll dynamics using eq. (12) is then given by

$$\begin{gathered}\dot{\boldsymbol{x}} = \boldsymbol{A}\boldsymbol{x} + \boldsymbol{B}\boldsymbol{\Lambda}(\boldsymbol{u} + \boldsymbol{\Theta}^\top \boldsymbol{\Phi}(\boldsymbol{x})), \\ \begin{bmatrix}\dot{\phi} \\ \dot{p}\end{bmatrix} = \begin{bmatrix}0 & 1 \\ 0 & a_1\end{bmatrix}\begin{bmatrix}\phi \\ p\end{bmatrix} + \begin{bmatrix}0 \\ 1\end{bmatrix}\lambda_1\left(\delta_a + \begin{bmatrix}\theta_{\text{bias, roll}}\end{bmatrix}\begin{bmatrix}1\end{bmatrix}\right),\end{gathered} \tag{13}$$

where $a_1 = -a_{\phi_1}$, $\lambda_1 = a_{\phi_2}$, $\theta_{\text{bias, roll}} = d_{\phi_2}$, and the pair $(\boldsymbol{A}, \boldsymbol{B}\boldsymbol{\Lambda})$ is controllable since the matrix $[\boldsymbol{B}\boldsymbol{\Lambda} \;\; \boldsymbol{A}\boldsymbol{B}\boldsymbol{\Lambda}]$ is of full rank for all $a_{\phi_2} \neq 0$.

Similarly, a linearization of the pitch dynamics is given by Beard & McLain [13] as

$$\dot{\theta} = q + d_{\theta_1}, \tag{14}$$

$$\ddot{\theta} = -a_{\theta_1}\dot{\theta} - a_{\theta_2}\theta + a_{\theta_3}\delta_e + d_{\theta_2}, \tag{15}$$

which gives the pitch model of the same form

$$\begin{gathered}\dot{\boldsymbol{x}} = \boldsymbol{A}\boldsymbol{x} + \boldsymbol{B}\boldsymbol{\Lambda}(\boldsymbol{u} + \boldsymbol{\Theta}^\top \boldsymbol{\Phi}(\boldsymbol{x})), \\ \begin{bmatrix}\dot{\theta} \\ \dot{q}\end{bmatrix} = \begin{bmatrix}0 & 1 \\ a_2 & a_3\end{bmatrix}\begin{bmatrix}\theta \\ q\end{bmatrix} + \begin{bmatrix}0 \\ 1\end{bmatrix}\lambda_2\left(\delta_e + \begin{bmatrix}\theta_{\text{bias, pitch}}\end{bmatrix}\begin{bmatrix}1\end{bmatrix}\right),\end{gathered} \tag{16}$$

where $a_2 = -a_{\theta_2}$, $a_3 = -a_{\theta_1}$, $\lambda_2 = a_{\theta_3}$ and $\theta_{\text{bias, pitch}} = d_{\theta_2}$, and the pair $(\boldsymbol{A}, \boldsymbol{B}\boldsymbol{\Lambda})$ is controllable since the matrix $[\boldsymbol{B}\boldsymbol{\Lambda} \;\; \boldsymbol{A}\boldsymbol{B}\boldsymbol{\Lambda}]$ is of full rank for all $a_{\theta_3} \neq 0$.

The bias terms in the model in eqs. (13) and (16) act as a steady state compensation, similar to an integral term in a PID controller.

B. Inner Loop PID Controllers

The PID controller for roll is given by

$$\delta_a = k_{p_\phi}(\phi^c - \phi) + \frac{k_{i_\phi}}{s}(\phi^c - \phi) - k_{d_\phi} p,$$

where ϕ^c is the commanded roll angle and k_{p_ϕ}, k_{i_ϕ} and k_{d_ϕ} are the control gains.

Similarly, the PID controller for pitch is given by

$$\delta_e = k_{p_\theta}(\theta^c - \theta) + \frac{k_{i_\theta}}{s}(\theta^c - \theta) - k_{d_\theta} q, \tag{17}$$

where θ^c is the commanded pitch angle and k_{p_θ}, k_{i_θ}, and k_{d_θ} are the control gains. This deviates from the pitch controller presented in [13], where the inner control loop in pitch does not include an integral term. This design choice of Beard & McLain [13] is to avoid limiting the bandwidth of the inner loop, based on the assumption that outer loop controllers will compensate for the steady state offset in pitch. In this paper, a key aspect is comparing the inner loop controllers of the MRAC and PID controllers without outer loop. As such, an integral term in the pitch control loop is added to compensate for a steady state offset in pitch.

The controller gains are given in table 2 in the Appendix.

C. Airspeed controller

The PI controller for airspeed control using throttle is given by [13]

$$\delta_t = \delta_t^* + k_{p_V}(V_a^c - V_a) + \frac{k_{i_V}}{s}(V_a^c - V_a), \tag{18}$$

where δ_t^* is the throttle trim value, and k_{p_V}, k_{i_V} are the control gains. The airspeed controller is used in both the PID and MRAC control schemes.

VI. Simulation Results

In this section, the simulation results are presented. The main limitations of the simulator are uncertainties related to the interpolation of the aerodynamic coefficients, and uncertainties concerning the extension to an asymmetric model. Additionally, stalling behavior is not implemented in the simulator. Consequently, every test run must be evaluated after running a simulation to assess if the angle of attack is within realistic values.

The icing level timeseries chosen for the simulations in Figs. 3, 4, and 7 is chosen to explore the response of the system under different icing configurations. The timeseries simulates the asymmetric build-up of icing, followed by de-icing of the right wing, a period of severe asymmetric icing, and finally de-icing of the left wing. Severe asymmetric icing refers to one wing being fully iced, while the other is clean.

The first 100 seconds of the simulations (not shown) the MRAC is excited by a signal consisting of a sum of sinusoids, to ensure that its internal states and parameters have converged to a suitable tuning before the icing events.

A. Tuning of MRAC

The solution, $\boldsymbol{P}$, to the Lyapunov equation in eq. (11) is included in each of the adaptive laws in eq. (10). Since the solution is given by

$$\boldsymbol{P} = \begin{bmatrix} \frac{q_2\omega_n^2+q_1+4q_1\zeta^2}{4\omega_n\zeta} & \frac{q_1}{2\omega_n^2} \\ \frac{q_1}{2\omega_n^2} & \frac{q_2\omega_n^2+q_1}{(q_2\omega_n^2+q_1)/(4\omega_n^3\zeta)} \end{bmatrix}, \tag{19}$$

where $\boldsymbol{Q}$ is chosen as

$$\boldsymbol{Q} = \begin{bmatrix} q_1 & 0 \\ 0 & q_2 \end{bmatrix},$$

and $\boldsymbol{A}_{\text{ref}}$ is chosen as

$$\boldsymbol{A}_{\text{ref}} = \begin{bmatrix} 0 & 1 \\ -\omega_n^2 & -2\zeta\omega_n \end{bmatrix},$$

the reference model and the choice of $\boldsymbol{Q}$ will affect all adaptations, $\hat{\boldsymbol{K}}_x$, $\hat{\boldsymbol{K}}_r$ and $\hat{\boldsymbol{\Theta}}$.

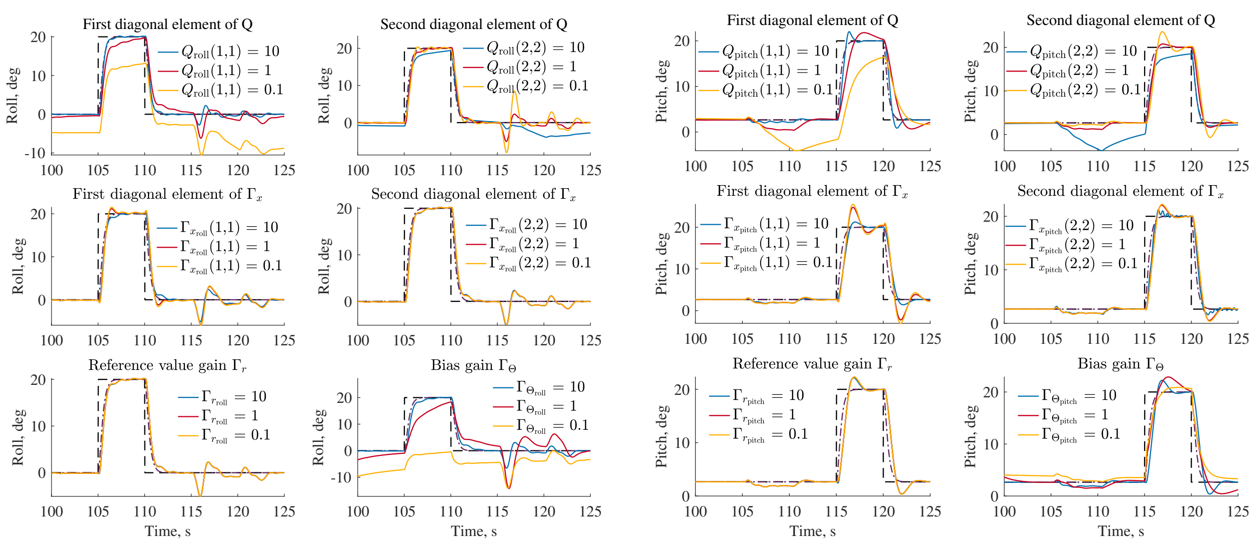

(a) The roll controller. From $t = 115$s to $t = 120$s the pitch reference (not shown) is set to $20°$.

(b) The pitch controller. From $t = 105$s to $t = 110$s the roll reference (not shown) is set to $20°$.

Figure 2 The effect of each of the adaptive rates. The icing level is set to $(\zeta_{\text{left}}, \zeta_{\text{right}}) = (0.8,\ 0.3)$.

Figures 2a and 2b illustrate how each adaptive rate affects the response of the systems. In each sub-figure a simulation is run with one adaptive rate set to the values $\{10, 1, 0.1\}$, while the other rates are constant. The adaptive rate in question for each sub-figure is given by the legend and title.

The value of the first diagonal element of the $\boldsymbol{Q}$-matrix, q_1, is seen in the upper left plot of Figs. 2a and 2b to have a significant impact on the tracking performance for both the roll and pitch controllers. This is expected as q_1 is present in every element of $\boldsymbol{P}$ given in eq. (19), wherein $\boldsymbol{P}$ is present in each of the adaptive laws in eq. (10).

Secondly, the adaptive rates $\boldsymbol{\Gamma}_x$ and $\boldsymbol{\Gamma}_r$ have considerably less impact on the response for both the roll and pitch controller. The central right plot in Fig. 2b shows, however, that an increase in the second diagonal element of $\boldsymbol{\Gamma}_x$ of the pitch controller leads to oscillations. With more aggressive pitch references and with increased asymmetry of the icing levels, these oscillations become more pronounced. As such, this gain value was chosen to be quite low.

Finally, Fig. 2a shows that the adaptive rate of the bias term in roll has a significant impact on the tracking performance. As mentioned in section V.A.1, the bias term acts as a steady state compensation. Likely. the term compensates for the additional roll moment produced by asymmetric icing levels, and thus plays a critical role in the tracking performance.

Overall, to avoid oscillations in the system states, the adaptive rates were chosen as small as possible while still ensuring adequate performance. The adaptive rates are given in table 1 in the Appendix.

B. Baseline Case

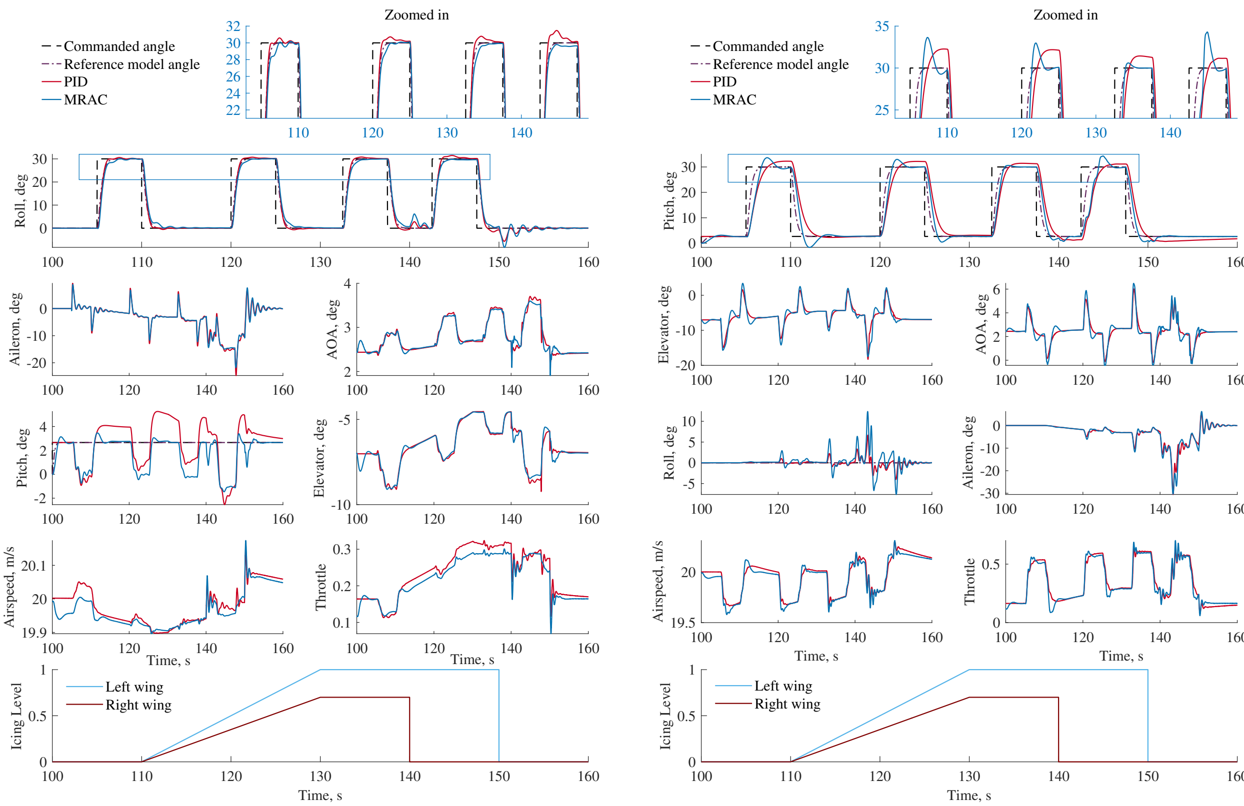

(a) Baseline simulation case with square reference signal in roll.

(b) Baseline simulation case with square reference signal in pitch.

Figure 3 The response of the baseline case with the adaptive controller and the PID controller is shown.

The baseline simulation case in Figs. 3a and 3b shows the response of the system with the MRAC and PID controllers run with a square reference in roll and pitch, respectively. The results show that both controllers perform well under different icing conditions with relatively aggressive reference angles in roll and pitch. Figure 3a shows an increase in throttle usage as the icing level increases, due to increased drag from the icing. The roll response in Fig. 3b shows an increase in the deviation from the zero degree roll reference as the simulation progresses.

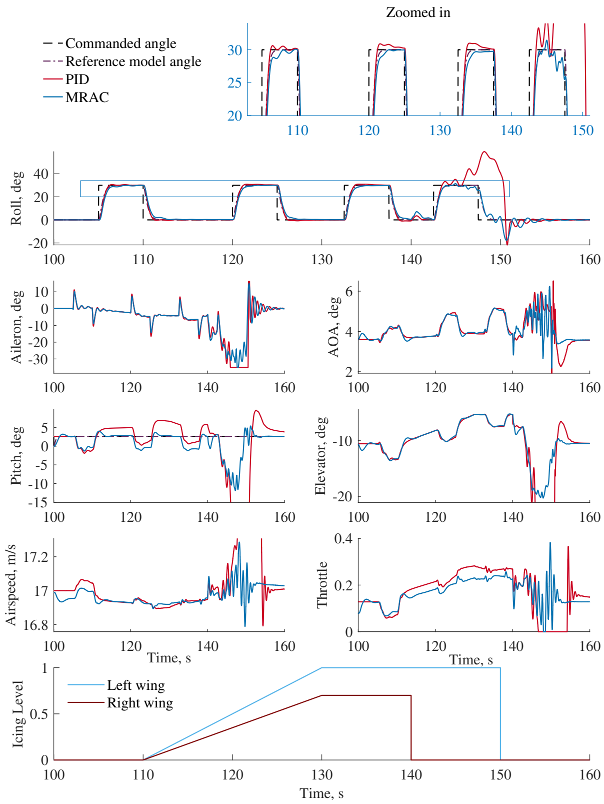

Figure 4 The response of the reduced airspeed case with $V_a = 17$m/s for the adaptive controller and the PID controller is shown.

C. Reduced airspeed

Figure 4 shows the response with the adaptive controller and the PID controller for the baseline case in Fig. 4 with the airspeed reduced from 20m/s to 17m/s. It can be seen that for the most severe icing phase from $t = 140$s to $t = 150$s where the icing is 100% asymmetric, the PID controller is not able to follow the roll reference. The roll angle reaches a maximum of 59° at $t \approx 148$s.

A simulation with the roll reference angle increased from $\phi_{\text{cmd}} = 30°$ to $\phi_{\text{cmd}} = 40°$ results in similar behavior for the adaptive controller as the PID controller in Fig. 4.

D. Reduced Control Surface Effectiveness

In Fig. 5 the system is simulated with a square reference signal in pitch using the reduced control surface efficiency found in the CFD analysis described in section IV. The results from applying this data is labeled "Reduction 1".

Additionally, a simulation with an even further reduction in the control surface effectiveness is run to test robustness, labeled "Reduction 2". The values for this simulation is given as follows: $C_{L_{\delta_e}}$ and $C_{l_{\delta_a}}$ are reduced by 50% from the clean to iced case, $C_{D_{\delta_e}}$ and $C_{n_{\delta_a}}$ are increased by 150% and $C_{m_{\delta_e}}$ is reduced by 50%.

Figure 5b shows that as the icing level increases, the response with the PID controller differs only slightly between the three levels of control surface effectiveness, indicating that the control effectiveness does not have any significant effect on the performance of the PID controller within this simulator framework. The adaptive controller in Fig. 5a experiences some increased overshoots in pitch and increased roll deviations with the reduction in control surface effectiveness.

Note how any significant deviation from the roll reference only occurs at $t \in (120, 140)$s, which coincides with asymmetric icing levels. When the icing level is symmetric with $\zeta = 0$ or $\zeta = 1$, the roll angle is much closer to its zero degree reference. A likely cause of this is that with asymmetric icing on the wings an additional roll moment is induced, throwing the UAV's balance off. As the icing level becomes symmetric again from $t = 143$s, the roll deviations diminish.

In Fig. 6 the system is simulated under the same conditions with reduced control surface effectiveness as described

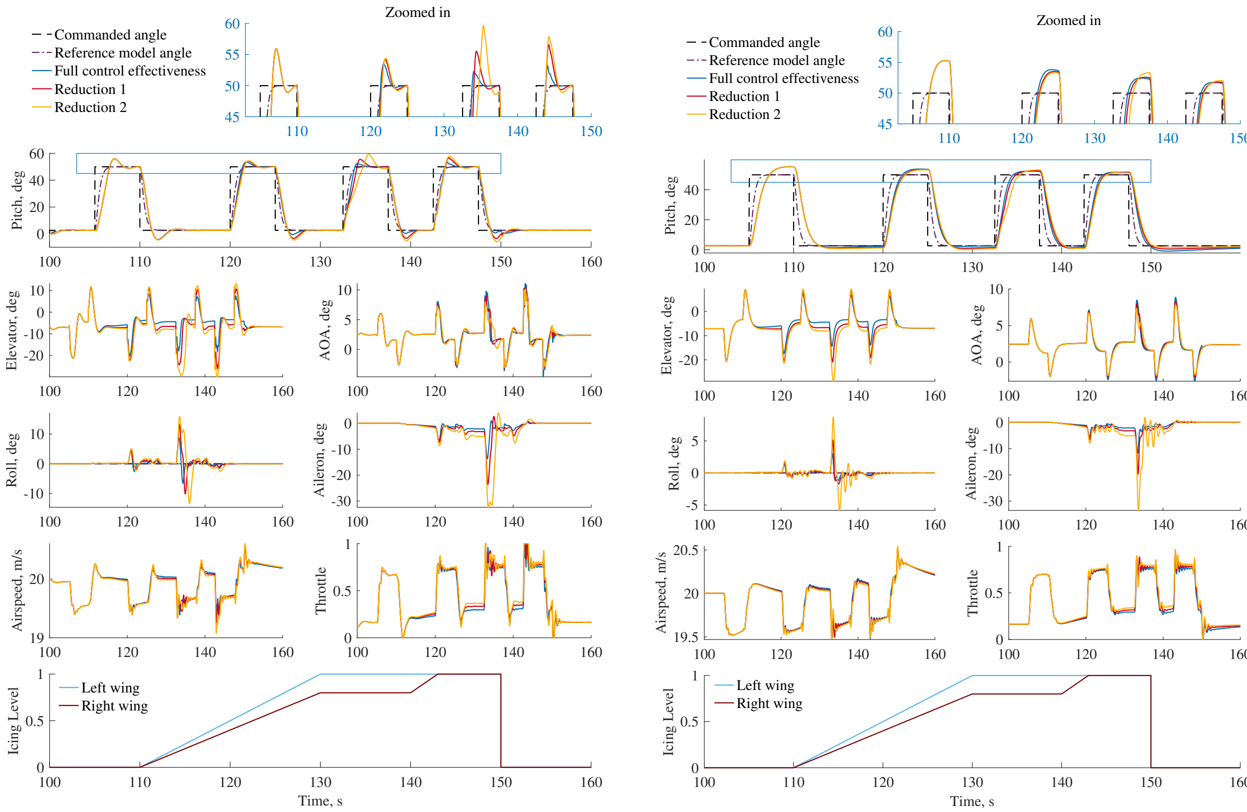

(a) Response with the MRAC controller. **(b) Response with the PID controller.**

Figure 5 Reduced control surface effectiveness simulation case with a 50° square reference signal in pitch. The response with with full control surface effectiveness, reduced control surface effectiveness according to the data of CFD simulations, and a case with a further reduction in control surface effectiveness is shown.

earlier in this section, with a square reference in roll instead of pitch.

The PID controller experiences increased deviations from the roll reference as the icing levels increase, whereas the MRAC controller appears less affected by the reduced control surface effectiveness.

E. Bias and Integral Terms

Figures 7a and 7b show a simulation case intended to investigate the bias terms of the adaptive controller and the integral terms of the PID controller. The motivation behind this simulation case is to examine whether the bias terms or the integral terms can detect the effects of the icing.

The first simulation in Fig. 7a (in blue) shows the response with the so-called "Original tuning", which corresponds to the tuning values of the adaptive controller given in table 1 in the Appendix. For the simulation labeled "Slower adaptation of bias" (in red) the adaptive rates of the bias terms have been lowered from $\Gamma_\Theta = 15$ to $\Gamma_\Theta = 1$ for the roll controller, and from $\Gamma_\Theta = 10$ to $\Gamma_\Theta = 1$ for the pitch controller. With the slower adaptive rate for the bias term, it is seen from Fig. 7a that the bias term, especially in roll, appears to follow the differential icing level. With the faster rate (in blue), the bias appears to be more influenced by the sideslip angle and angle of attack.

Similarly, the simulation labeled "Original tuning" (in blue) in Fig. 7b is run with the tuning values of the PID controller given in table 2 in the Appendix. For the simulation labeled "Alternative tuning" (red), the integral terms are changed from $k_{i_\phi} = 2$ to $k_{i_\phi} = 0.5$, and $k_{i_\theta} = -0.1$ to $k_{i_\theta} = -0.3$. The tuning values of the "Alternative tuning" case were found by attempting to tune the integral terms to closer match the differential and sum of the icing level. The integral term in roll was lowered, resulting in less peaks from $t = 100$s to $t = 135$s. However, that also resulted in a slower response in the integral term during the largest peak in the differential icing level at $t \in (135, 145)$s. The integral term in pitch in Fig. 7b is increased slightly from its "original" tuning as the integral term looked to be too slow to

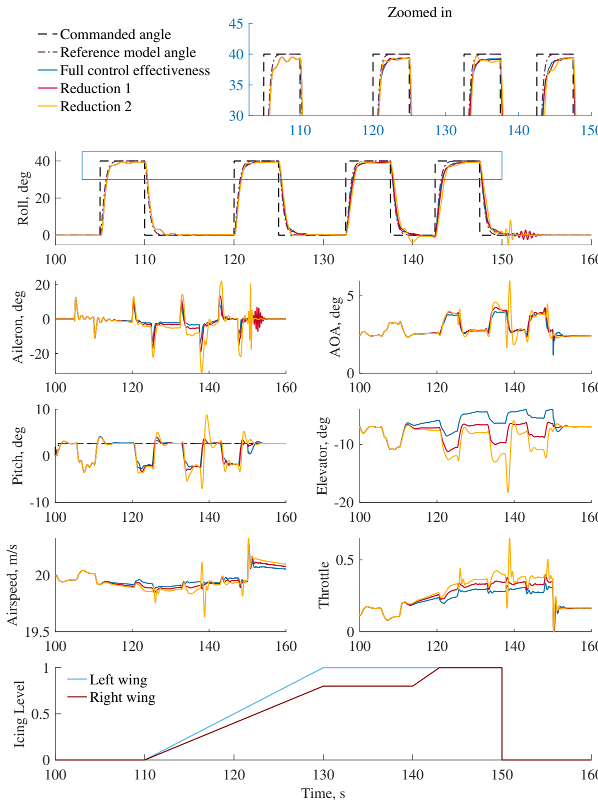

(a) **Response with the MRAC controller.**

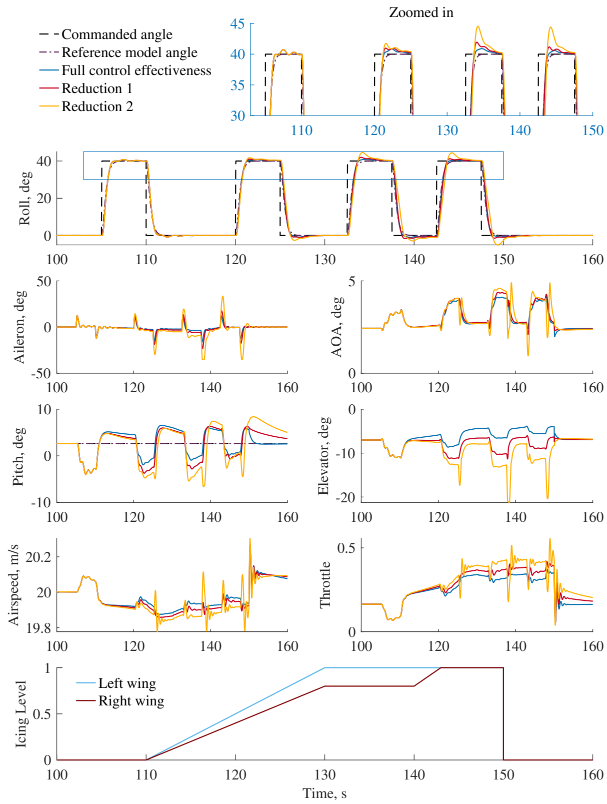

(b) **Response with the PID controller.**

Figure 6 Reduced control surface effectiveness simulation case with a 40° square reference signal in roll. The response with with full control surface effectiveness, reduced control surface effectiveness according to the data of CFD simulations, and a case with a further reduction in control surface effectiveness is shown.

capture the sum of the icing levels. However, neither increasing nor decreasing k_{i_θ} resulted in significantly increased similarity to the sum of the icing levels.

VII. Discussion

A. Stalling

For the simulations in this paper, the modelling by Winter *et al.* [10] and the extension to an asymmetric aerodynamic model by Kleiven *et al.* [6] has been assumed to be valid. Winter *et al.* [10] suggests a stall limit in the fully iced case of $\alpha_{\text{stall}} \approx 10°$. However, the CFD analysis in section VIII.A, suggests that the stall limit is closer to $\alpha_{\text{stall}} \approx 4°$ in the fully iced case. The reason for this discrepancy could stem from the differences in the configurations in the CFD simulations from the configuration used in Winter et al., such as variations in chord length and hinge location, and the fact that the airfoil of the Skywalker X8 is unknown and that the two approximations may reflect different behaviour.

As mentioned in section IV, the CFD analysis is only used to find an estimate of the reduction in control surface effectiveness from the clean case to the fully iced case. Nevertheless, due to the great uncertainty in the stall limit for the iced case, the values of the angle of attack and stalling of the UAV have not been the focus in this paper. More work must be done to determine accurate ranges for the stall limit in icing.

B. Effects of icing

The results in section VI show that the 100% asymmetric icing case, i.e. when the left wing is fully iced and the right wing is clean, is the most severe icing case with respect to the performance of the controllers. The greater the asymmetry, the greater the coupling of the roll and pitch dynamics is. An example of the increase in coupling between

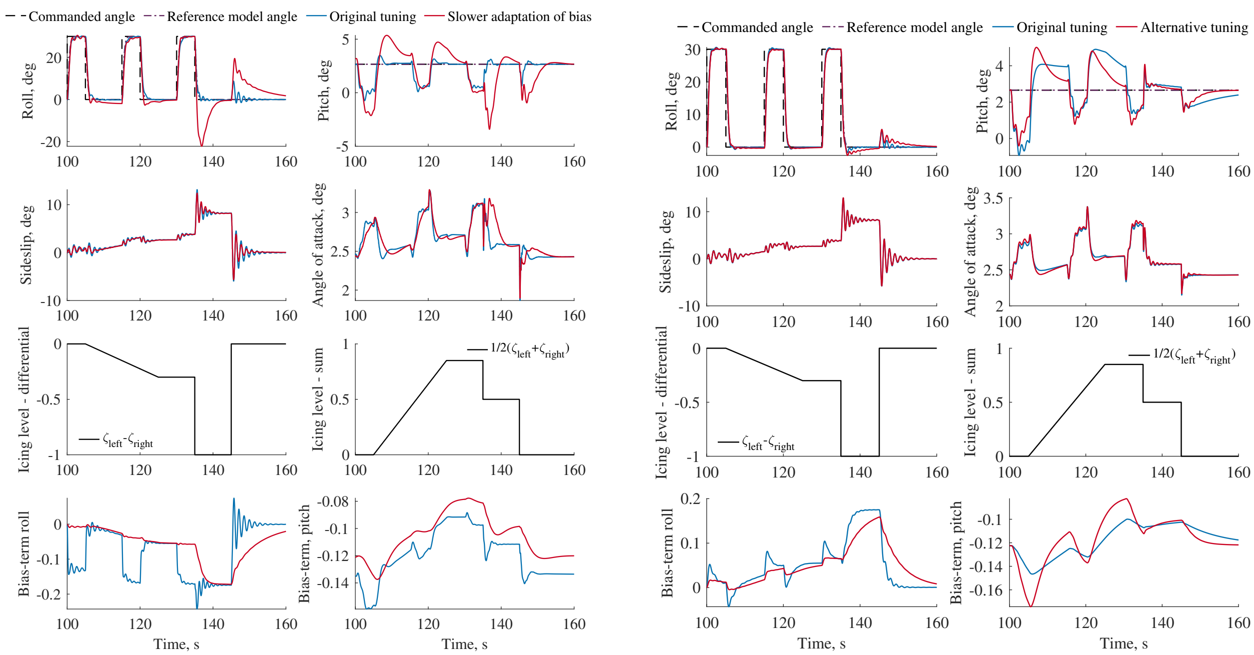

(a) MRAC controller. **(b) PID controller.**

Figure 7 The bias terms of the MRAC controller, and the integral terms of the PID controller.

the two states with increased asymmetry is observed as the deviations from the zero degree reference in roll during pitch deflections are larger for increased asymmetry, observed in Figs. 5b and 3b.

The reduced control surface effectiveness simulation case with a pitch angle reference in Fig. 5, shows that the pitch response with MRAC controller is more affected by the changes in control surface effectiveness than the PID controller. With the square roll angle reference in Fig. 6, the opposite is true, where the roll response with the PID controller is more affected by the changes in control surface effectiveness than the MRAC controller.

C. Bias and integral terms

From the examination of the bias terms in section VI.E, there is an indication that a bias term might be able to detect the icing levels of the airfoils. However, for faster adaptive rates the bias terms seem to also capture the effects of the sideslip angle and the angle of attack, and perhaps additional unmodelled effects.

Some further work on this might be able to produce an estimate of the icing levels, which would be very beneficial for the development of ice protection systems. Some paths forward with this could be modifying the MRAC model equations in an attempt to separate the icing effects from other unmodelled effects. During the design of the regressor, $\mathbf{\Phi}(\boldsymbol{x})$, one could choose to include compensating linear terms in the sideslip and angle of attack, and thereby infer the effect of these through their respective adaptive parameters. That is, setting $f(\boldsymbol{x})$ in eq. (7) to $[\theta_{\text{bias,roll}} \;\; \theta_\beta][1 \;\; \beta]^\top$ in the the roll model equations, and to $[\theta_{\text{bias,pitch}} \;\; \theta_\alpha][1 \;\; \alpha]^\top$ in the the pitch model equations. This would be especially pertinent seeing how these terms appear in the full equations of motion of an aircraft in [13]. In this paper, sideslip angle and angle of attack were deliberately not included in the regessor since these quantities are difficult to measure accurately for a UAV [14]. Nonetheless, a significant challenge in continuing down this path will be to produce a *reliable* estimate of the icing level across several atmospheric conditions and flight scenarios.

VIII. Conclusion

This paper has investigated inner loop adaptive control of the Skywalker X8 fixed-wing UAV in icing conditions. An MRAC control scheme has been implemented and its performance compared with a PID controller. The MRAC model was chosen as a linear model with a bias term to capture additional unmodelled effects. Through several simulation cases, it was found that the performance of the MRAC and PID were quite similar. However, the MRAC performs better in the case of reduced airspeed for asymmetric icing levels. By modifying the tuning, the bias terms of the MRAC control scheme, and to some degree the integral terms of the PID controller, are able to capture the icing levels on the airfoils of the UAV.

Computational fluid dynamics analysis allowed for a realistic simulation of the reduced control surface effectiveness due to icing. The results show that the MRAC controller is less affected by the reduction in control surface efficiency than the PID control scheme with a square reference angle in roll, while the opposite is true with a square reference angle in pitch. There is uncertainty in the stall limit of the UAV in icing conditions, and consequently more work must be done to determine accurate ranges for the stall limit in icing.

As a concluding remark, it is noted that the MRAC control scheme is more complex and introduces more tuning parameters than the PID control scheme - while they prove similar performance, with the MRAC performing better under certain conditions as discussed in this paper. Additionally, with the increased complexity and the system identification aspect of the MRAC scheme comes the possibility of exploring icing level estimation.

Appendix

A. Control surface CFD icing simulations

The effect of ice accretions on control surface effectiveness was estimated using icing CFD methods. A series of simulations were performed with ANSYS FENSAP-ICE (version 2021 R1) in 2D on a reconstructed airfoil of the X8. The airfoil chord was set to 45cm with a flap hinge at 80% of the chord length and deflection angles of 0°, 10° and 20°.

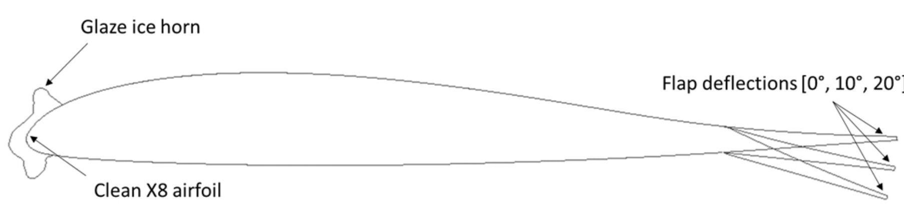

Figure 8 Cross section of the ice shape.

These geometries were generated for a clean (uniced) airfoil as baseline and an iced airfoil – resulting in a total of six geometries, see Fig. 8. The ice shape used for this case is based on an earlier work and represent a severe icing case with a very distinct horn [5]. While the ice shape was obtained using legacy methods, it can still be considered as a realistic case. It represents a severe glaze horn with a complex geometry, that is not unlike geometries that have been generated with more modern methods [3]. The ice shape can conditions can be interpreted as typical worst case scenario. For each of the six geometries, lift, drag, and moments were simulated over a range of angles of attack. The FENSAP-ICE simulations were conducted with a Spalart-Allmaras turbulence model with upwind artificial viscosity. More details about the numerical simulation parameters and meshing settings are described in previous work and were identical in this study [3].

The results for lift, drag, and moments over angle of attack are shown in Fig. 9. The results on the clean airfoils show the typical aerodynamic behavior of flaps. An increase of the flap deflection angle leads to an increase in lift, increase in drag, and reduction in stall angle. Since a flap deflection leads to additional lift generated near the trailing-edge of the airfoil, it generates additional nose-down moment. In principle, the same behavior occours for the iced airfoils. The largest difference is an substantially earlier onset of stall of the iced airfoils compared to the clean cases. The offset seems constant (i.e. independent from flap deflection angle) with a angle of attack difference of $-11°$. This behavior can be explained by the large leading-edge separation bubble that is induced by the ice horn, see Fig. 10. This separation bubble increases the turbulence in the downstream flow and substantially decreases its resistance against stall at even moderate angles of attack.

In addition to this earlier stall, the results in Fig. 9a also show that the iced airfoils generate less lift than the clean airfoil and also less additional lift per degree of flap deflection. Figure 9b shows that the iced airfoils generate substantially more drag compared to the clean airfoils. Also, the additional drag generated from the flaps is larger compared to clean airfoil flaps. In average, the flaps on the iced airfoil generate -27% less lift and $+86\%$ more drag

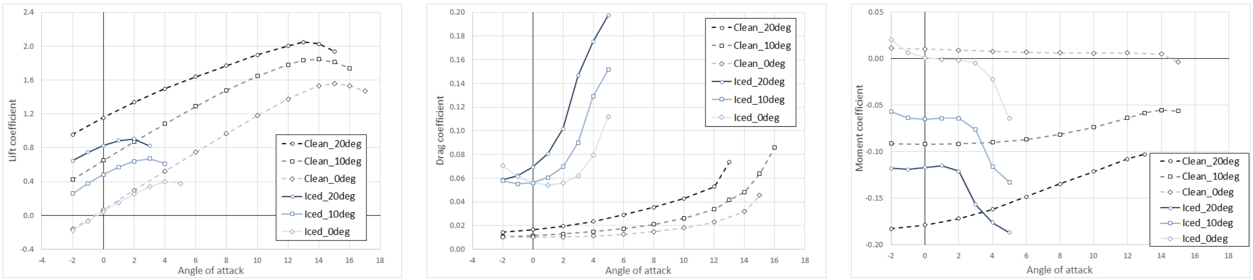

(a) Results for lift. **(b) Results for drag.** **(c) Results for moments.**

Figure 9 The results for lift, drag, and moments over angle of attack.

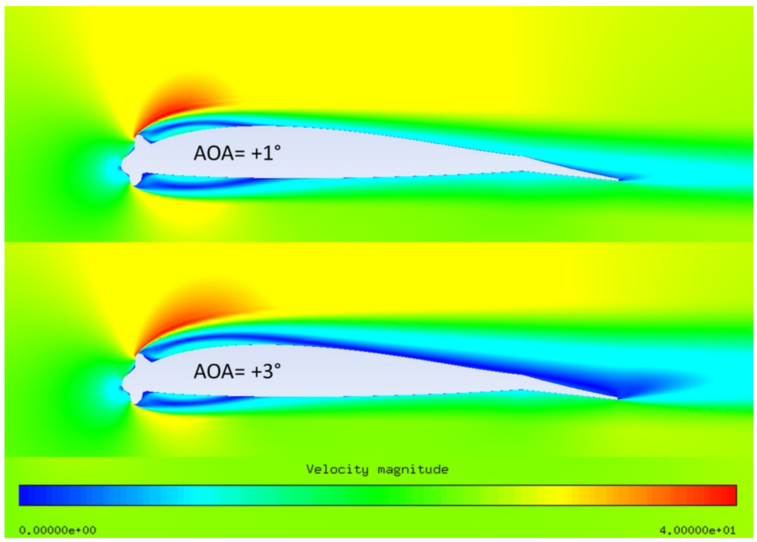

Figure 10 Flow separation on the leading edge.

per angle of deflection compared to the clean airfoil. The effect of ice on the moment behavior is shown in Fig. 9c. The effects here are less consistent compared to drag and lift. Without any flap deflection, the iced airfoil generates slightly less moment, resulting almost in a neutral airfoil. In the cases with flap deflection, the iced airfoils generate more positive moments. In average, the iced airfoils generates −37% less moment compared to the clean case.

In summary, the analysis show show that icing has several critical effects on the airfoil. Ice accretions decrease the effectiveness of the control surface by lowering the additional lift and increasing the additional drag per degree of flap deflection. While icing also leads to a substantial reduction of the stall angles, the CFD analysis is only used to find an estimate of the reduction in control surface effectiveness from the clean case to the fully iced case in this paper. Furthermore, the ice shape is leading to substantial changes in the moment behavior, which can affect the overall aircraft stability.

B. Controller parameters

Acknowledgments

The work is partly sponsored by the Research Council of Norway through the Centre of Excellence funding scheme, project number 223254, AMOS, and projects number 316425, and 296228.

The numerical simulations were performed on resources provided by the National Infrastructure for High Performance Computing and Data Storage in Norway (UNINETT Sigma2) on the Fram supercomputer, under project code NN9613K Notur/NorStore"

Table 1 The adaptive rates of the MRAC scheme.

Roll adaptive rates		Pitch adaptive rates	
Parameter	Value	Parameter	Value
$\boldsymbol{Q}$	$\begin{bmatrix} 3 & 0 \\ 0 & 1 \end{bmatrix}$	$\boldsymbol{Q}$	$\begin{bmatrix} 4 & 0 \\ 0 & 0.4 \end{bmatrix}$
$\boldsymbol{\Gamma}_x$	$\begin{bmatrix} 12 & 0 \\ 0 & 4 \end{bmatrix}$	$\boldsymbol{\Gamma}_x$	$\begin{bmatrix} 6 & 0 \\ 0 & 0.01 \end{bmatrix}$
$\boldsymbol{\Gamma}_r$	10	$\boldsymbol{\Gamma}_r$	5
$\boldsymbol{\Gamma}_\Theta$	15	$\boldsymbol{\Gamma}_\Theta$	10

Table 2 The tuning parameters of the roll and pitch PID controllers.

Roll controller gains		Pitch controller gains	
Parameter	Value	Parameter	Value
k_{p_ϕ}	2.5	k_{p_θ}	-1
k_{i_ϕ}	2	k_{i_θ}	-0.1
k_{d_ϕ}	0.01	k_{d_θ}	-0.25

References

[1] Bragg, M., Broeren, A., and Blumenthal, L., "Iced-airfoil aerodynamics," *Progress in Aerospace Sciences*, Vol. 41, No. 5, 2005, pp. 323–362. https://doi.org/https://doi.org/10.1016/j.paerosci.2005.07.001.

[2] Lynch, F. T., and Khodadoust, A., "Effects of ice accretions on aircraft aerodynamics," *Progress in Aerospace Sciences*, Vol. 37, No. 8, 2001, pp. 669–767. https://doi.org/10.1016/S0376-0421(01)00018-5.

[3] Hann, R., and Johansen, T. A., "UAV icing: the influence of airspeed and chord length on performance degradation," *Aircraft Engineering and Aerospace Technology*, Vol. 93, 2021. https://doi.org/10.1108/AEAT-06-2020-0127.

[4] Hann, R., Enache, A., Nielsen, M. C., Stovner, B. N., van Beeck, J., Johansen, T. A., and Borup, K. T., "Experimental heat loads for electrothermal anti-icing and de-icing on UAVs," *Aerospace*, Vol. 8, 2021. https://doi.org/10.3390/aerospace8030083.

[5] Hann, R., "Atmospheric Ice Accretions, Aerodynamic Icing Penalties, and Ice Protection Systems on Unmanned Aerial Vehicles." Ph.D. thesis, Norwegian University of Science and Technology, 2020.

[6] Kleiven, R., Gryte, K., and Johansen, T. A., "Robust and Gain-Scheduled Flight Control of Fixed-Wing UAVs in Wind and Icing Conditions," *IEEE Aerospace Conference*, 2021.

[7] Ioannou, P. A., and Sun, J., *Robust adaptive control*, Dover Publications, Inc, Mineola, New York, 2012.

[8] Chowdhary, G., Johnson, E. N., Chandramohan, R., Kimbrell, M. S., and Calise, A., "Guidance and Control of Airplanes Under Actuator Failures and Severe Structural Damage," *Journal of Guidance, Control, and Dynamics*, Vol. 36, No. 4, 2013, pp. 1093–1104. https://doi.org/10.2514/1.58028.

[9] Lavretsky, E., and Wise, K. A., *Robust and adaptive control: with aerospace applications*, Advanced textbooks in control and signal processing, Springer, London ; New York, 2013. OCLC: ocn837660452.

[10] Winter, A., Hann, R., Wenz, A., Gryte, K., and Johansen, T. A., "Stability of a Flying Wing UAV in Icing Conditions," *8th European Conference for Aeronautics and Space Sciences (EUCASS)*, 2019.

[11] Liu, Y., Li, L., Chen, W., Tian, W., and Hu, H., "An experimental study on the aerodynamic performance degradation of a UAS propeller model induced by ice accretion process," *Experimental Thermal and Fluid Science*, Vol. 102, 2019, pp. 101–112. https://doi.org/https://doi.org/10.1016/j.expthermflusci.2018.11.008.

[12] Hann, R., Wenz, A., Gryte, K., and Johansen, T. A., "Impact of atmospheric icing on UAV aerodynamic performance," *2017 Workshop on Research, Education and Development of Unmanned Aerial Systems (RED-UAS)*, IEEE, Linkoping, 2017, pp. 66–71. https://doi.org/10.1109/RED-UAS.2017.8101645.

[13] Beard, R. W., and McLain, T. W., *Small Unmanned Aircraft: Theory and Practice*, Princeton University Press, USA, 2012.

[14] Wenz, A., and Johansen, T. A., "Moving Horizon Estimation of Air Data Parameters for UAVs," *IEEE Transactions on Aerospace and Electronic Systems*, Vol. 56, No. 3, 2020, pp. 2101–2121. https://doi.org/10.1109/TAES.2019.2946677.